Identify of flow patterns in bubbling fluidization

Li, Yunning; Fan, Hui; Fan, Xianfeng

DOI:
10.1016/j.ces.2014.07.012

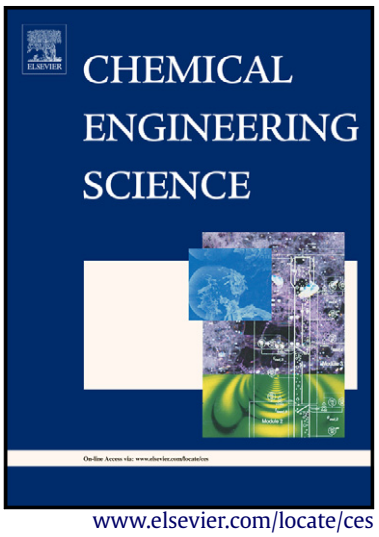

www.elsevier.com/locate/ces

Identify of Flow Patterns in Bubbling Fluidization

Yunning Li, Hui Fan, Xiangfeng Fan

PII: S0009-2509(14)00357-1
DOI: http://dx.doi.org/10.1016/j.ces.2014.07.012
Reference: CES11745

To appear in: *Chemical Engineering Science*

Received date: 3 April 2014
Revised date: 4 July 2014
Accepted date: 10 July 2014

Cite this article as: Yunning Li, Hui Fan, Xiangfeng Fan, Identify of Flow Patterns in Bubbling Fluidization, *Chemical Engineering Science,* http://dx.doi.org/10.1016/j.ces.2014.07.012

Identify of Flow Patterns in Bubbling Fluidization

Yunning Li[a], Hui Fan[b], Xiangfeng Fan[a*],

[a] Institute for Materials and Processes, School of Engineering, The University of Edinburgh, Edinburgh EH9 3JL, UK
[b] College of Medical and Dental Sciences, The University of Birmingham, Birmingham B15 2TT, UK

Abstract

Bubbling fluidization has been widely applied in process industries, such as power generation from coal, renewable energy production, gasification and pyrolysis. In this study, we attempted to predict solid flow patterns in a bubbling fluidized bed based on operational conditions, the air distributor and particle velocity. We first investigated the effect of operational conditions and the air distributor on solid/gas flow patterns, and the correlations between solid/gas flow patterns with the solid mixing, solid and gas contact, and bubble behaviour within bubbling fluidized beds by using positron emission particle tracking (PEPT). A 'Flow Pattern Parameter (FPP)' is then proposed to identify the solid flow pattern in a bubbling fluidized bed. The 'Flow Pattern Parameter (FPP)' consists of particle kinetic energy, bed aspect ratio (H/D), pore size of air distributor, minimum fluidization velocity, and superficial gas velocity. The results show that solid flow patterns in the bubbling fluidized bed can be clearly classified based on the Flow Pattern Parameter. Different flow pattern corresponds to a certain range of the Flow Pattern Parameter.

Keywords: Bubbling fluidization; flow structure; air distributor; superficial gas velocity; solid properties

[*]Corresponding author. Tel.: +44(0)1316505678. E-mail address: x.fan@ed.ac.uk

1. Introduction

Bubbling fluidization has been employed to many industrial processes, such as coal combustion and gasification, renewable energy production, chemical, petrochemical and metallurgical processes, granulation and drying (Di Maio et al., 2013; Salman and Hounslow, 2007). It has been demonstrated that the reaction efficiency, heat transfer and energy consumption in bubbling fluidization depend on solid mixing, solid-gas contact (Clift and Seville, 1993; He et al., 2004; Shibata et al., 1991), while solid mixing and solid and gas contact further depend on solid/gas flow structure or solid/gas flow pattern. Intensive research has been conducted to investigate the fluidization behaviour experimentally and numerically (Cloete et al., 2013; Gómez-Barea and Leckner, 2010; Herzog et al., 2012; Salman and Hounslow, 2007; Shi et al., 2011; Wardag and Larachi, 2012; Xiong et al., 2011), and many models have been developed for optimizing reactor design and bed scale up, and for identifying the effect of operational conditions, particle properties and bed design on fluidization behaviour. For example, Li et al proposed an energy minimization multi-scale model (EMMS) to characterize the meso-scale structure of fluidization (Shi et al., 2011). Xiong et al proposed a smoothed particle hydrodynamics method to solve problems in modelling dense particle–fluid fluidization (Xiong et al., 2011). Herzog et al used different CFD-codes to predict pressure drop and bed expansion ratio in a gas-solid fluidized bed by considering solid-phase properties, momentum exchange coefficients (Herzog et al., 2012). Ku et al used an Eulerian-Lagrangian approach to simulate a bubbling fluidized bed and analysed solid flow pattern, bed expansion, pressure drop and fluctuation by considering drag force correlations, particle-particle and particle-wall collisions (Ku et al., 2013). Wang et al developed a drag model to simulate the meso-scale structure in solid-gas bubbling fluidized beds. Their simulated results have

a good agreement with experimental data (Wang et al., 2013). Olsson et al experimentally investigated the fuel dispersion in a large scale bubbling fluidized bed with a cross section area of 1.44 m^2 through analysing the effect of operational conditions and fuel particle properties on the local mixing mechanisms and lateral fuel dispersion (Olsson et al., 2012). Fotovat et al investigated the gas distribution in a bubbling fluidized bed and the effect of solid loading and biomass quantity on bubble void fraction and distribution (Fotovat et al., 2013). Vakhshouri and Grace found that fluidization models have always neglected the effect of plenum chamber volume on fluidization behaviour and experimentally investigated its effect on the behaviour of FCC and glass particle bed (Vakhshouri and Grace, 2010).

However many factors can affect solid/gas flow pattern in a fluidized bed and make fundamental analysis, modelling and prediction of fluidization behaviour difficult and in some cases impossible. In a fluidized bed, gas flow is introduced into a bed through a gas distributor and forms many bubbles or voids. The bubbles or voids drive solid particles circulating around within the bed (Garcia-Gutierrez et al., 2013; Laverman et al., 2012; Soria-Verdugo et al., 2011). The circulation pattern is determined by the bubble size, bubble rise velocity, and bubble distribution within the bed, which further depend on superficial gas velocity, pore size of air distributor, density and size of solid particles, column diameter etc. All of these factors are interrelated, but we do not know their relative importance (Ding et al., 2006). For example, bubbles drive particles, and the moving particles interact with bed wall and packed particles, in turn the interaction between particles and bubbles affect the macroscopic and microscopic behaviour of the bed, bubble size, bubble rise velocity, and bubble distribution (Ding et al., 2006; Smolders and Baeyens, 2001; Wang et al., 2011).

Several experimental techniques have also been developed to measure and analyse the fluidization behaviour and the effect of various factors, such as positron emission particle tracking technique (PEPT) (Laverman et al., 2012; Parker et al., 1997; Parker et al., 1993), X-ray densitometry/tomography (Saayman et al., 2013), electrical capacitance volume tomography (Weber and Mei, 2013), ultra-fast magnetic resonance imaging, the measurement of pressure fluctuations (Sedighikamal and Zarghami, 2013), LDV measurement and analysis of gas and particulate phase velocity profiles (Mychkovsky and Ceccio, 2012), laser Doppler anemometry (LDA), cross-sectional wire mess sensors.

In this study, we use PEPT to directly measure the impact of the operation parameters and air distributor on solid and gas behaviour in a bubbling fluidized bed. We will investigate the effect of aspect ratio (H/D), pore size of air distributor, and superficial gas velocity on fluidization, and then provide a form of equation to identify the flow structure in bubbling fluidization regime based on bed design and operational conditions.

2. Positron Emission Particle Tracking (PEPT) Technique

The Positron emission particle tracking (PEPT) has been developed to track lubricant flow in aircraft engines at the University of Birmingham in 1980'. Recent development has extended its application to track 1-3 particles in opaque vessels or dense systems accurately and non-invasively, to study multiphase flow, such as granular materials and viscous fluid flows, in engineering processes. The technique employed 1-3 radioactively labelled particles and a pair of positron-sensitive γ-ray detectors to receive the γ-rays emitting from tracer particles. An iterative algorithm has also been developed to calculate the tracer positions (Yang et al., 2007a; Yang et

al., 2007b). The tracer particles are normally labelled by ^{18}F, ^{61}Cu or ^{66}Ga. These radioisotopes decay via β^+ decay and emit positrons. The positron rapidly annihilates with an electron and gives γ-rays. In PEPT technique, we are interested in the γ-rays with energy of 511 keV because they emit in pair and as counterpropagating γ-rays. Theoretically, all the counterpropagating γ-rays should meet at a point in space where the tracer particle is located (Fig. 1). The two detectors designed to capture γ-ray pairs simultaneously and the tracer locations can be defined from the collected γ-ray pairs. In practice, many γ-rays are corrupted, and lines connecting the two ends of counterpropagating γ-rays which are detected by the two detectors do not pass the tracer source. Therefore, the location algorithm (Yang et al., 2007a; Yang et al., 2007b) has been developed to discard the corrupted γ-ray events and calculate the actual tracer position.

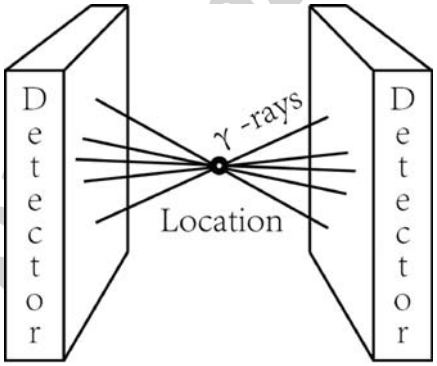

Figure 1. Schematic diagram of PEPT

The location algorithm starts from calculating the distances of a point perpendicular to the all gamma ray trajectories, and then finds the point that minimises the sum of the distances (Yang et al., 2007a; Yang et al., 2007b). For example, for a giving set of γ-ray M, the sequential trajectories named as M_1 … M_N, the summation of distances from point (x, y, z) to all γ-ray trajectories is:

$$D_M(x,y,z)=\sum_s d_i(x,y,z)\ \text{(mm)} \tag{1}$$

The minimum solution for the sum of distance is then obtained from

$$\begin{cases}\dfrac{\partial D_M(x,y,z)}{\partial x}=0\\ \dfrac{\partial D_M(x,y,z)}{\partial y}=0\\ \dfrac{\partial D_M(x,y,z)}{\partial z}=0\end{cases} \tag{2}$$

The first approximation of the minimum distance from the point (x_0, y_0, z_0) can be calculated based on Eq. (2) with a mean deviation of

$$\delta_M(x_0,y_0,z_0)=\frac{D_M(x_0,y_0,z_0)}{N(M)}\ \text{(mm)} \tag{3}$$

Where $\delta_i(x,y,z)$ is the distance between point (x,y,z) and the i^{th} trajectory; $N(M)$ is the events number in the set M.

The distance of the point (x_0, y_0, z_0) to all trajectories within the set M are calculated and each trajectory with a distance $d_i(x_0,y_0,z_0)$ larger than $k\,\delta_s(x_0,y_0,z_0)$ is discarded, here k is a constant. After discarding the corrupt events, more accurate tracer location (x_1,y_1,z_1) can be calculated using the subset events M_1 with a renewed mean difference of $\delta_{s1}(x_1,y_1,z_1)$. Following the same iteration principle process, and discarding the corrupted events in each selecting subsets M_2, M_3 etc. until a specified fraction of the initial trajectories (f) remaining, the iteration is finished. The calculated tracer location is actually the point (x_F,y_F,z_F) with a minimum distance to the uncorrupted trajectories within the event set M, or the minimum distance to the final subset event M_F within the time interval covered by the

event set M. Every single event M_i has its own time of measurement t_i recorded, and the location calculated is representing the particle's position at time

$$t = \frac{1}{N_F} \sum_{M_F} t_i \text{ (s)} \tag{4}$$

Where $N_F \equiv N(S_F)$ is the number of trajectories in the final subset S_F.

3. Material and methods

PEPT measurements were carried out using the Birmingham positron camera (Fan et al., 2008b). The camera comprised of two rectangular gamma detectors with a maximum separation distance of 750 mm. Each detector has an active area of 500×400 mm^2 which can covers the section of bubbling fluidized bed used in this study. The camera can record γ-ray pairs emitted from the labelled tracer particles at a speed up to 100,000 γ-ray pairs per second.

The fluidization experiments were performed in a Plexiglas cylindrical bed. The bed has an inner diameter of 152 mm and a height of 1 m. The bed materials were fluidized by an air flow from a GA11CFF air compressor at ambient temperature. The air flow rate was regulated using calibrated rotameters. Experiments were designed to investigate the effect of the aspect ratio (H/D), superficial gas velocity, and air distributor on solid/gas flow structure. The air distributors were sintered metal sheets with pore diameters varying from 1 μm to 15 μm, and stainless steel wire mesh sheets with the pore diameters varying from 60 μm to 230 μm. The air distributor made from sintered metal has open area ratio from 24 to 28%. For the air distributor with a pore size of 60μm, the wire diameter was 40.6 μm, and the open area ratio was 36%. For the air distributor with a pore size of 230 μm, the wire diameter and the open area ratio were 190.5 μm and 30%, respectively. The pressure under the air distributor was

in a range from 3.3 to 4 bars, which can make sure that the bed fluidized uniformly. The pressure drops across the air distributor were less than 8%.

The bed materials were glass beads with the average diameter of 352 microns, and a size range from 300-400 μm. The density of glass beads was 2700 (kg/m^3). The total mass of the packed bed was 4 kg, 6 kg or 8 kg, which were correspond to the bed aspect ratios of 1, 1.5 and 2 units, respectively. The glass beads used in this study belong to group B in terms of Geldart classification and its minimum fluidization velocity was determined to be 0.15 m/s. The applied superficial gas velocity varied from 0.31 m/s to 0.64 m/s. The operation conditions and bed configurations for all experiments presented in this paper can be found in table 1. The experiments were performed within the bubbling fluidization regime that was characterized by visual observation and the measured bed pressure drop.

In order to represent the fluidization behaviour of the bulk material, glass beads with an average size of around 352 μm were randomly selected from the bulk material and radioactively labelled using ^{18}F as tracers. The ^{18}F was produced from double deionised water by using the MC40 Cyclotron from the Birmingham University. Under the bombardment of a 33MeV ^{3}He beam, a tiny fraction of the oxygen atoms in water was converted to ^{18}F in the form of fluoride ions through the reactions of $^{16}O(^{3}He, n)^{18}Ne \rightarrow ^{18}F$ and $^{16}O(^{3}He, p)^{18}F$. The capacity to absorb ^{18}F from the radioactive water of glass beads was poor, therefore their surfaces were modified by metallic ions in aqueous solution previous to the labelling. The metallic ions played as a bridge to enhance the adsorption of ^{18}F. After the modification, the radioactivity labelled to a single glass bead increased from 2 to 400 μCi, which gave sufficient γ-ray pairs for smooth tracking the particle motion. The detailed procedure for labelling

glass beads using ^{18}F radioisotope can be seen in (Fan et al., 2006a, b; Fan et al., 2006c).

In PEPT experiments, we tracked one glass bead. To ensure the measured data representing the behaviour of the bulk and to avoid errors, each experiment was run for 2 hours to allow the labelled particle passing throughout the bed. The solid flow pattern is plotted based on the average vector graphics using the accumulative tracking data which recorded the particle locations in roughly every 5 milliseconds. As shown in Fig. 2, the experimental set-up consisted of a 3-D gas-solid fluidized bed and the PEPT system.

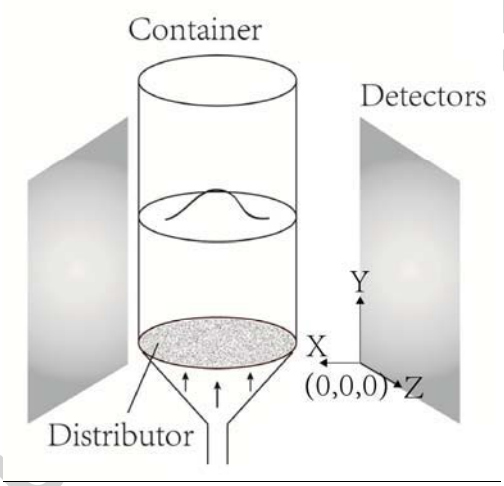

Figure 2. Schematic diagram of the experimental set-up.

Table 1 Operation conditions and bed configurations

Experiments	Pore size of air distributor (μm)	Superifical gas velocity (m/s)	Aspect ratio (H/D)	Flow pattern
1	230	0.64	1	B
2	230	0.57	1	B
3	230	0.49	1	B
4	230	0.40	1	A
5	230	0.31	1	A
6	60	0.57	1	A
7	60	0.49	1	A
8	60	0.40	1	A
9	60	0.31	1	A
10	60	0.57	1.5	A
11	60	0.49	1.5	A
12	15	0.57	1	A
13	15	0.49	1	A
14	15	0.40	1	A
15	15	0.31	1	A
16	15	0.57	2	C
17	15	0.40	2	C
18	10	0.57	2	C
19	10	0.40	2	C
20	1	0.57	1	D
21	1	0.40	1	D
22	1	0.57	1.5	D

23	1	0.40	1.5	D
24	1	0.57	2	D
25	1	0.40	2	D

4. Results and Discussion

4.1 Solid flow structure in fluidized beds

PEPT experiments were conducted under various experimental conditions to investigate the effect of air distributors, the bed aspect ratio (H/D), and superficial gas velocities on the solid/gas flow structure in a bubbling fluidized bed. Four flow patterns, which are named as patterns A, B, C and D, were observed in this study as shown in Fig. 3. Patterns A, B and D were observed when the bed material was 300-400 glass beads and the ratio of bed height to bed diameter was unit, and have been discussed previously (Fan et al., 2008a; Fan et al., 2011; Fan et al., 2008b).

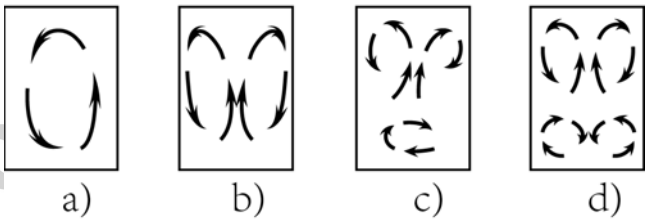

Figure 3. Solid flow structures in bubbling fluidized beds observed by PEPT camera.

In general, pattern D was observed when the pore size of air distributor was 1 μm and superficial gas velocity was equal or greater than 0.4 m/s. Pattern C was observed when the pore size of air distributor was between 10 μm and 15 μm, the fixed bed height was 2 units of the bed diameter, and the superficial gas velocity was equal or greater than 0.4 m/s. Pattern B was observed when the pore size of air distributor was

230 μm and the superficial gas velocity was 0.49 - 0.64 m/s. Pattern A was observed when the pore size of air distributor was between 15 and 230 μm.

Figure 4 shows the overall flow pattern from the view of x-y plane and z-y plane, and gives vertical velocity map of glass beads in different bed levels for pattern A which shows particles moving upwards and downwards. The data indicates that pattern A gave a large circulation cell and covered the whole bed. The glass beads circulated upwards at right-hand side of the bed and moved down to the bottom along the left-hand side. Pattern A was observed when the pore size of air distributor was between 15 and 230 μm. It also varies with superficial gas velocity. For the detail, please see Table 1. The pattern A has been considered as a poor flow pattern since particles at bottom edge of the bed hardly moved, but it can reveal the effect of the superficial gas velocity, the pore size of air distributors, and the bed aspect ratio (H/D) on solid/bubble flow structures.

Figure 5 shows the solid flow pattern B and the upward velocity map of glass beads at different bed levels. This pattern has been reported and used frequently to validate the modelling and simulation work in literatures. In pattern B, upward and downwards glass beads were well distributed through the whole cross section of the bed immediately above the air distributor at a relatively uniform velocity. The uniform vertical velocity indicates that the gas travelled up at relative uniform velocity, and the gas distribution and bubble sizes were uniform. At the high layer of the bed, the upward glass beads moved inwards and travelled to the splash zone along the central region. The glass beads always moved down to the bottom along the bed annulus. Pattern B was observed when the pore size of air distributor was 230 μm and the superficial gas velocity was 0.49 - 0.64 m/s.

The pattern C (Fig. 6) was observed when the pore size of air distributor was between 10 μm and 15 μm, the fixed bed height was 2 units of the bed diameter, and the superficial gas velocity was equal or greater than 0.4 m/s. Three solid circulation cells were observed in this pattern, where one circulation cell was at the bottom section of the bed and two circulation cells at the top section. In the intermediate section, the solid flow behaviour was fairly complex. The downward solid flow met with bottom solid flow, resulting in an enhanced mixing and redistribution of the solids to top and bottom sections.

Pattern D (Fig. 7) was observed when the pore size of air distributor was 1 μm and superficial gas velocity was equal or greater than 0.4 m/s. The fluidized bed can be seen as three sections. The four symmetrical circulation cells were allocated in top section and bottom section. When the air flow was introduced into the fluidized bed, the air drove glass beads moving upwards along the bed annulus, and circulated down in the central region. The tracked glass bead hardly travelled upwards through the central region of the bottom section within the two-hour experiment. Solid flow pattern in the top section of the bed was similar to the flow pattern observed in the pattern B. Glass beads travelled upwards along the central axis of the bed, and then circulated back to the middle section of the bed along the bed annulus. In the intermediate section of the bed, the glass bead flow from the bottom section encountered with the glass bead flow from the top section of the bed in the annulus. The collision of two glass-bead flows pushed particles inwards the bed centre, and enhanced the particle mixing. The collision of two glass flows also split air bubbles to smaller size and gave a longer bubble residence time, therefore enhancing solid-gas contact. After the enhanced mixing, glass beads were redistributed to the bottom circulation and top circulation. The particle collision and the downward solid flow in

the main gas stream may also cause some gas back mixing which reduces the process efficiency.

The deviations between upward and downward fluxes in measured layers were evaluated in order to assess the technique performance. The maximum and minimum were found out of 3.6% and 0% respectively, and the average error turned out to be 1.5%. This confirmed that the technique can well represent the solid fluxes within the bed.

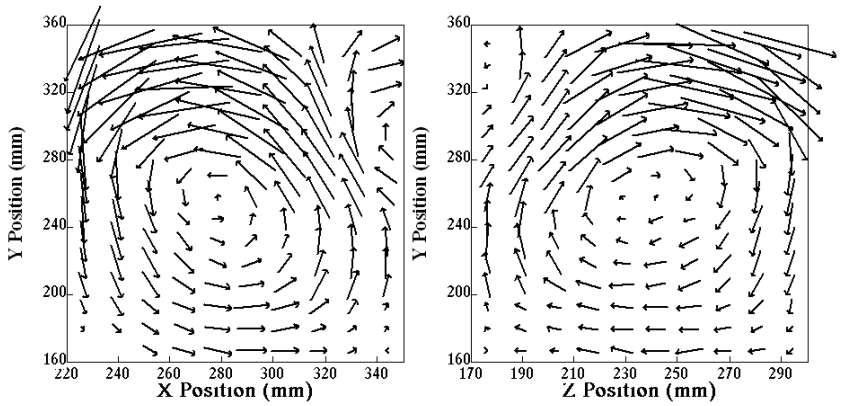

(a)

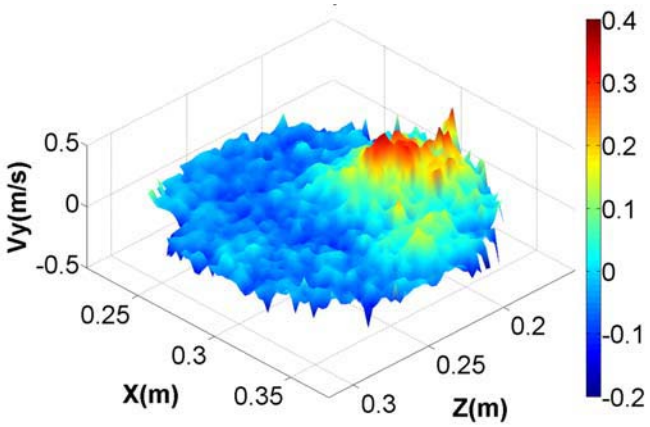

(b)

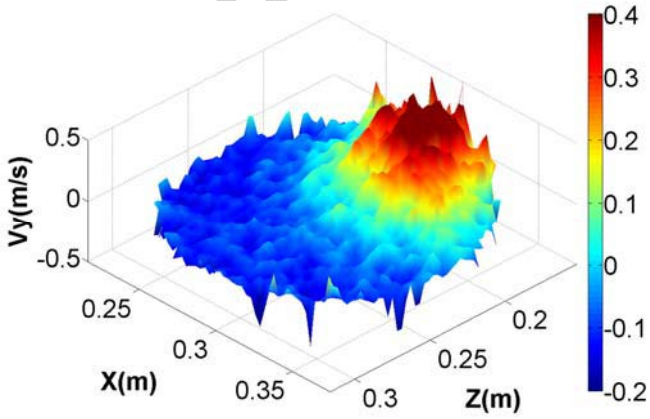

(c)

Figure 4. Flow pattern A. (a) overall time-averaged velocity vector map of solid from the view of x-y plane and z-y plane, (b) solid vertical velocity map in a 30-mm layer just above the air distributor (y=195mm, 35 mm above the air distributor), (c) solid vertical velocity map in a 30-mm layer in the intermediate bed section (y=250mm, 90mm above the air distributor).

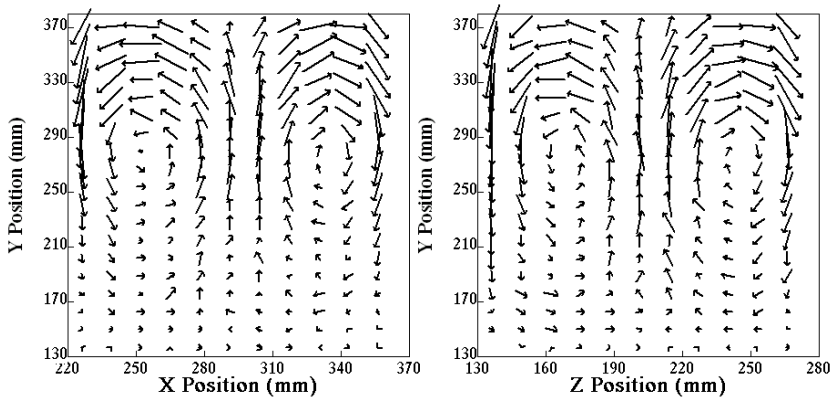

(a)

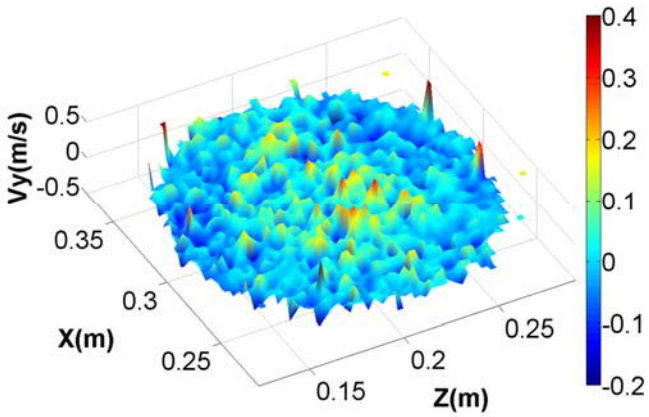

(b)

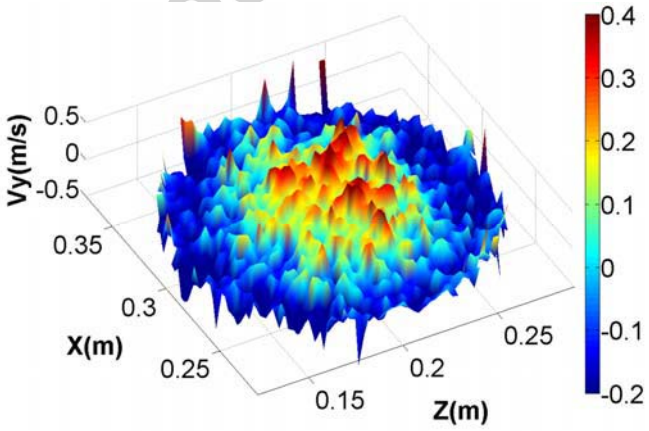

(c)

Figure 5. Flow pattern B. (a) overall time-averaged velocity vector map of solid from the view of x-y plane and z-y plane, (b) solid vertical velocity map in a 30-mm layer just above the air distributor (y=165mm, 35mm above the air distributor), (c) solid vertical velocity map in a 30-mm layer in the intermediate section (y=225 mm, 90mm above the air distributor).

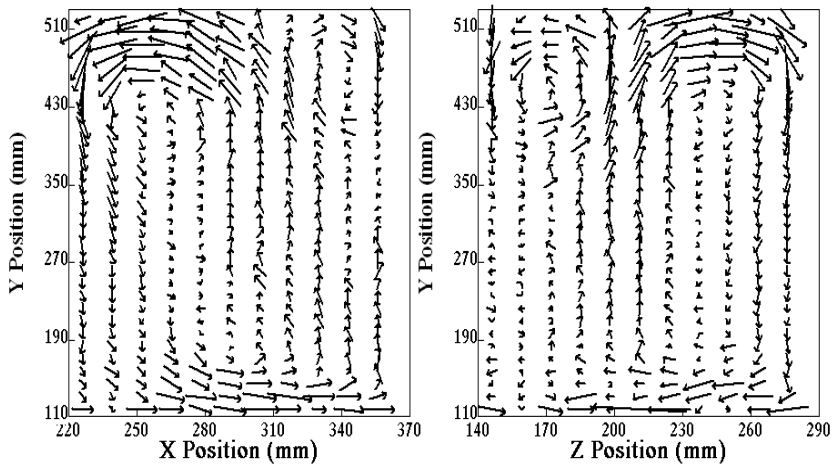

(a)

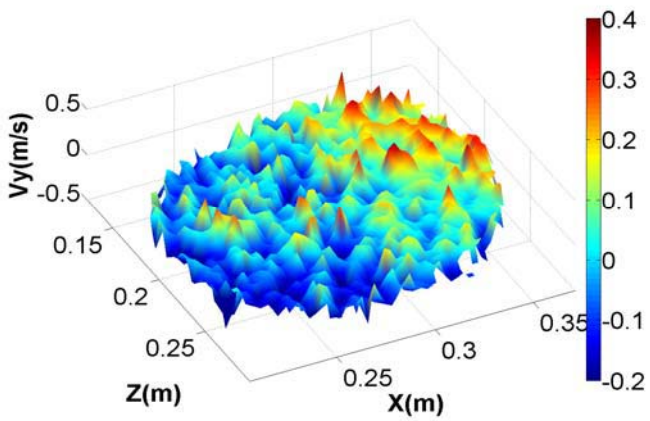

(b)

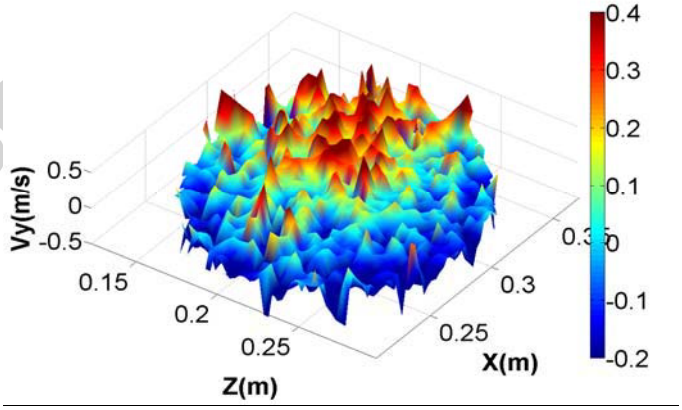

(c)

Figure 6. Flow pattern C. (a) overall time-averaged velocity vector map of solid from the view of x-y plane and z-y plane, (b) solid vertical velocity map in a 30-mm layer just above the air distributor (y=160mm, 50mm above the air distributor), (c) solid vertical velocity map in a 30-mm layer in the intermediate section of the bed (y=270mm, 160mm above the air distributor).

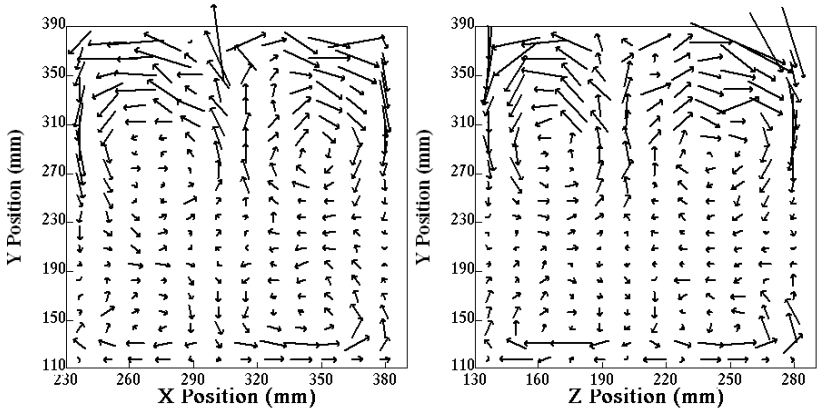
Y Position (mm)
390
350
310
270
230
190
150
110
230
260
290
320
350
380
X Position (mm)
Y Position (mm)
390
350
310
270
230
190
150
110
130
160
190
220
250
280
Z Position (mm)

(a)

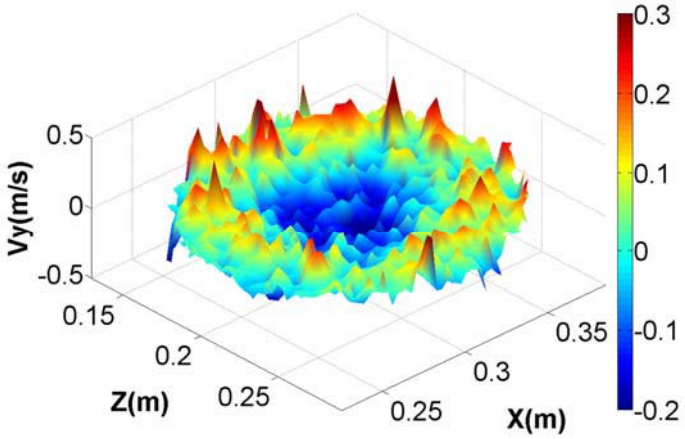
Vy(m/s)
0.5
0
-0.5
0.15
0.2
0.25
Z(m)
0.25
0.3
0.35
X(m)
0.3
0.2
0.1
0
-0.1
-0.2

(b)

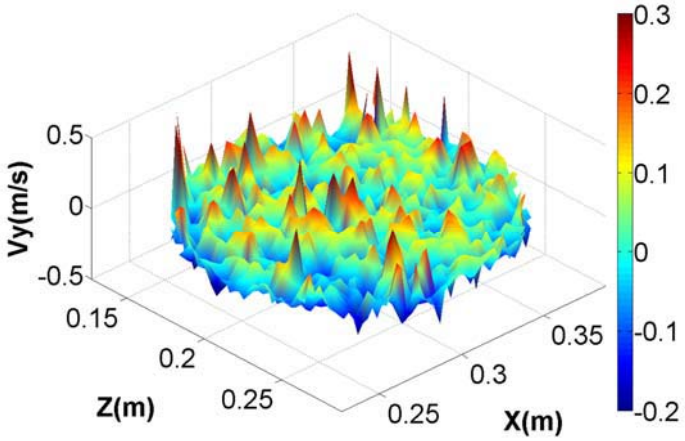
Vy(m/s)
0.5
0
-0.5
0.15
0.2
0.25
Z(m)
0.25
0.3
0.35
X(m)
0.3
0.2
0.1
0
-0.1
-0.2

(c)

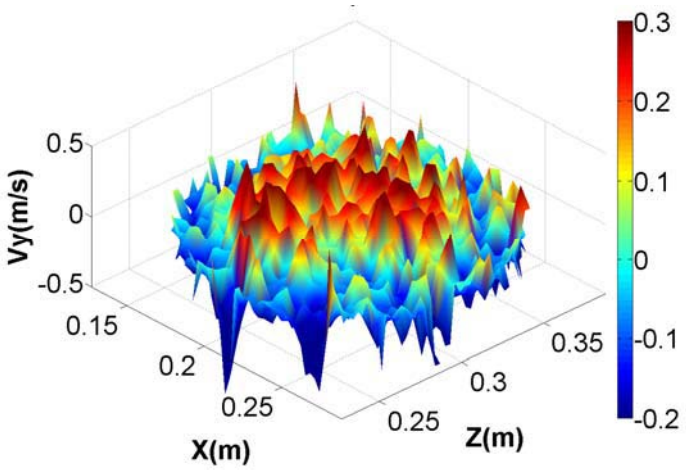

(d)

Figure 7. Flow pattern D. (a) overall time-averaged velocity vector map of solid from the view of x-y plane and z-y plane, (b) solid vertical velocity map in a 30-mm layer just above the air distributor (y=145mm, 35mm above the air distributor), (c) solid vertical velocity map in a 30-mm layer at an intermediate height of the bed (y=200mm, 90mm above the air distributor), (d) solid vertical velocity map in a 30-mm layer in the top section of the bed (y=270mm, 160mm above the air distributor).

Figures 8 and 9 show the bubble rise velocities in the fluidized beds, which were calculated from the PEPT data or using the correlations proposed by Mori & Wen, and Davidson & Harrison (Kunii and Levenspiel, 1991). The calculation of bubble rise velocity and bubble size based on PEPT data has been discussed in our previous publication (Fan et al., 2008b). To calculate the bubble rise velocity (U_b) using the correlation proposed by Davidson and Harrison (Eq 5.), the bubble sizes were firstly calculated using the correlation from Mori & Wen (Eq. 6)

$$u_b = 0.711(gd_b)^{1/2} \text{ (cm/s)} \quad (5)$$

$$d_b = d_{bm} - (d_{bm} - d_{b0}) \times e^{-0.3z/D} \text{ (cm)} \quad (6)$$

Where u_b is the rise velocity of a bubble (cm/s), g is the acceleration of gravity (cm/s^2), d_b is the bubble diameter (cm), d_{bm} is the maximum bubble diameter (cm), d_{b0} is the bubble diameter just above the air distributor (cm), z is the distance above the air distributor (cm), and D is the bed diameter (cm).

$$d_{b0} = \frac{2.78}{g}\left(u - u_{mf}\right)^2 \text{ (cm)} \tag{7}$$

$$d_{bm} = 0.65\left[\frac{\pi}{4}D^2\left(u - u_{mf}\right)\right]^{0.4} \text{ (cm)} \tag{8}$$

Where u is the superficial gas velocity (cm/s), u_{mf} is the minimum fluidization velocity (cm/s).

From Figures 8 and 9, it can be seen that the bubble rise velocities calculated from PEPT data were, in general, in agreement with the results calculated from the correlations proposed by Mori & Wen, and Davidson & Harrison. The difference is that the empirical correlations cannot reflect the bubble splitting in the middle section the beds for flow patterns C and D. The approach for calculating the bubble rise velocity in a bed from the PEPT data can be successfully applied.

In patterns A and B, bubble rising velocity increased dramatically with the bed height (Fan et al., 2008a; Fan et al., 2011). In pattern D, the bubble rising velocity increased gradually for a certain height in the bottom section, decreased at the intermediate section, and then increased again at the top section. The decrease in the bubble rising velocity within the intermediate section was due to the collision of upward and downward solid flows. The collision split the bubbles; therefore, bubble rising velocity reduced. The bubbles coalesced in the top section, and their rising velocity increased again. Bubbles in pattern A and B were large and rose rapidly whereas bubbles in patterns D were smaller and rose slowly. Pattern C was only observed in fluidized beds higher than 1.5 bed diameter. Fig. 9 is the bubble rising velocity for patterns C and D in the beds with the aspect ratio of 2 units. It can be observed that the bubble rise velocity in the bed with an aspect of 2 was different from the rise velocity in a bed with an aspect of 1. In pattern C, the bubble rise velocity increased gradually for the first 90 mm in the bottom section, and kept as a

constant value for about 180 mm in height, and then increased again. The unchanged situation in the bubble rise velocity within the intermediate section might due to the splitting of some bubbles, which resulted in the time-averaged bubble rise velocity unchanged. The bubble rising velocity in pattern D in a bed with the aspect ratio of 2 units was similar to that in a bed with the aspect ratio of unit, whereas there was a flat section in the velocity profile. The bubble rising velocity increased at the bottom section of the bed, and kept constant for a distance of about 80 mm then decreased due to the collision of solid flows as discussed previously.

Overall, flow pattern D gives the best solid mixing and solid-gas contact, while Pattern A gives the lowest mixing efficiency and solid-gas contact.

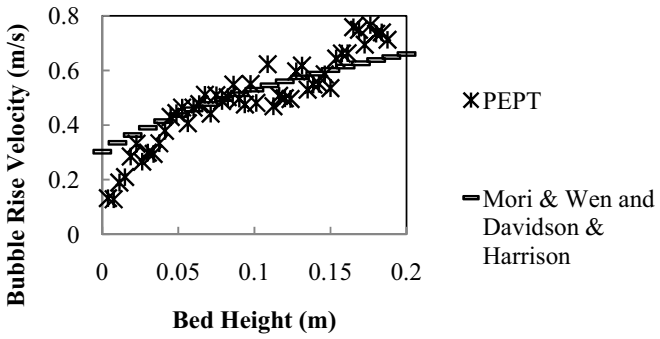

(a) Pattern A (d_D=60μm, u=0.57m/s)

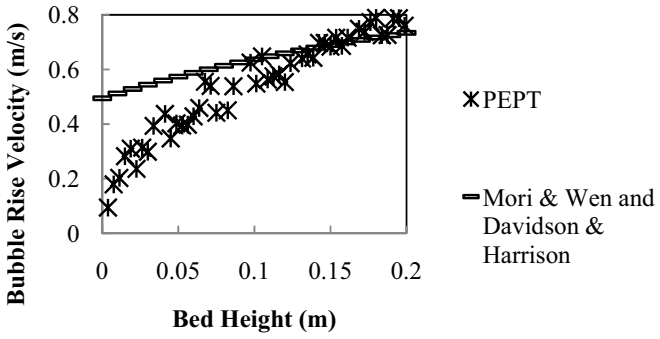

(b) Pattern B (d_D=230μm, u=0.57m/s)

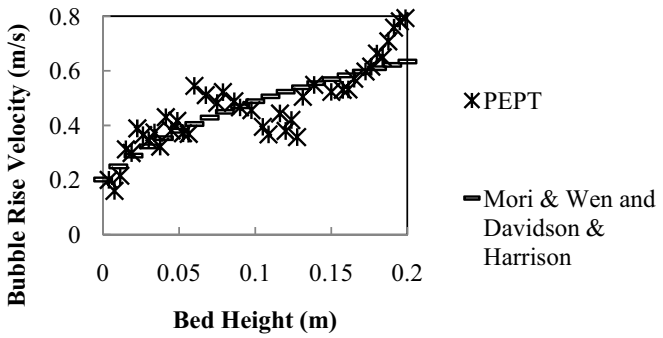

(c) Pattern D (d_D=1μm, u=0.57m/s)

Figure 8. Bubble rise velocity in a fluidized bed with the H/D of 1 unit.

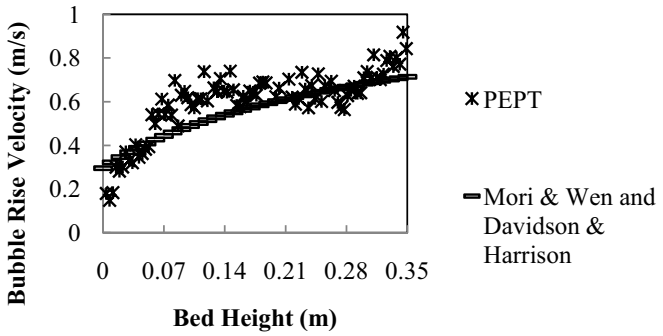

(a) Pattern C (d_D=15μm, u=0.40m/s)

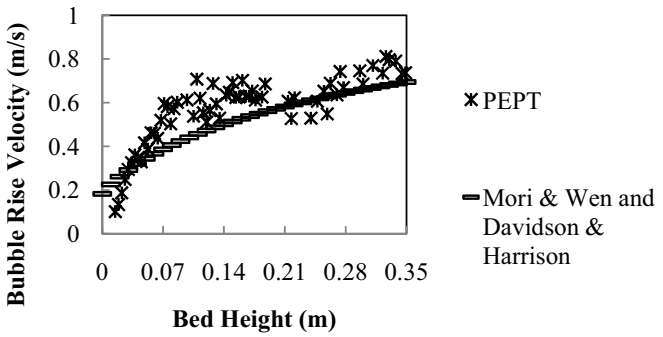

(b) Pattern D (d_D=1μm, u=0.40m/s)

Figure 9. Bubble rise velocity in a fluidized bed with the H/D of 2 units.

4.2 Identify Flow Pattern Parameter

The PEPT data have shown that solid flow patterns in a bubbling fluidized bed are controlled by the superficial gas velocity, the bed aspect ratio, and the pore size of the air distributor. Each flow structure is a result of the combination of various factors. In this section, attempts are made to identify the solid flow patterns in a 3D bubbling fluidized bed based on operational conditions, bed design and particle velocity.

In order to find out the conditions under which different flow pattern was formed, a number of PEPT experiments have been conducted to analyse the effects of superficial gas velocity, bed aspect ratio, and the pore size of the air distributors on the flow patterns. The experimental results were then classified into 4 groups based on their flow pattern. Investigations started from the measurement of the particle kinetic energy for glass-bead beds (Fig. 10), because the particle kinetic energy has been considered as an important factor related to the flow patterns, particularly the particle kinetic energy around the bottom section of the bed. Figure 10 shows how the kinetic energy per unit mass particle (v^2) varies with the bed height in the four flow patterns. The results indicate that particle kinetic energy is not the only factor affecting the solid flow patterns. The solid flow patterns cannot be classified only based on the difference in the particle kinetic energy. In order to identify certain flow patterns for Geldart B particle beds, a 'Flow Pattern Parameter (FPP)' has been proposed based on the PEPT measurement. The FPP takes account of particle kinetic energy, minimum fluidization velocity, superficial gas velocity, the pore size of the air distributor, bed diameter to the bed height ratio. The form of FPP is given as below,

$$FPP = \frac{H}{D} \cdot \sqrt{\frac{v^2}{d_D^{\,4} \times \left(u - u_{mf}\right)^2}} = \frac{H}{D} \cdot \frac{|v|}{d_D^{\,2} \times \left(u - u_{mf}\right)} \ (1/\mathrm{mm}^2) \qquad (9)$$

Where H is the height of fixed bed (mm), D is the bed diameter (mm), v is the particle speed (mm/s), d_D is the pore diameter of air distributor (mm), u is the superficial gas velocity (mm/s), u_{mf} is the minimum fluidization velocity (mm/s).

The FPP was calculated based on all experimental data from the fluidized bed with a diameter of 152 mm and packed glass-bead beds of 150-300 mm. Figure 11 shows the relationship between the FPP value and the solid flow patterns. From Figure 11, it can be seen that the solid flow patterns can be clearly separated via FPP, and each flow patterns fall into a specific FPP range. Pattern B can be found when the FPP is greater than 10 but less than 40 ($1/mm^2$). Pattern A can be found when the FPP is between 40 ($1/mm^2$) and 1.5×10^4 ($1/mm^2$). Pattern C can be found when the FPP is between 1.5×10^4 ($1/mm^2$) and 5×10^4 ($1/mm^2$), and the pattern D can be found when the FPP is larger than 8×10^5 but less than 5×10^6 ($1/mm^2$).

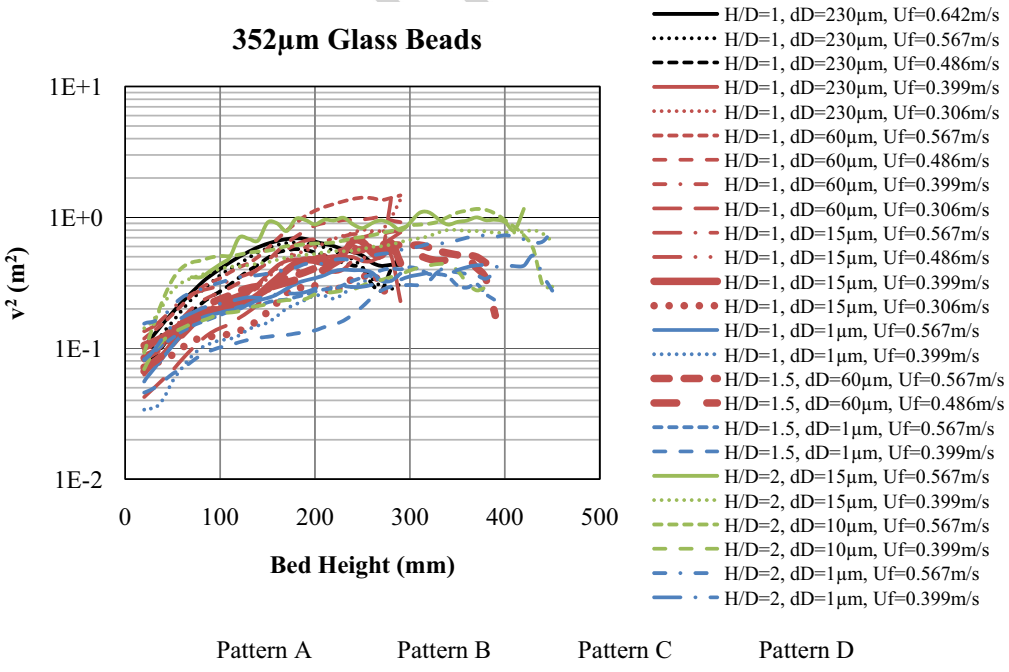

Figure 10. Kinetic energy per unit mass vs. bed height for glass beads with a size of 352 microns in the bubbling fluidization.

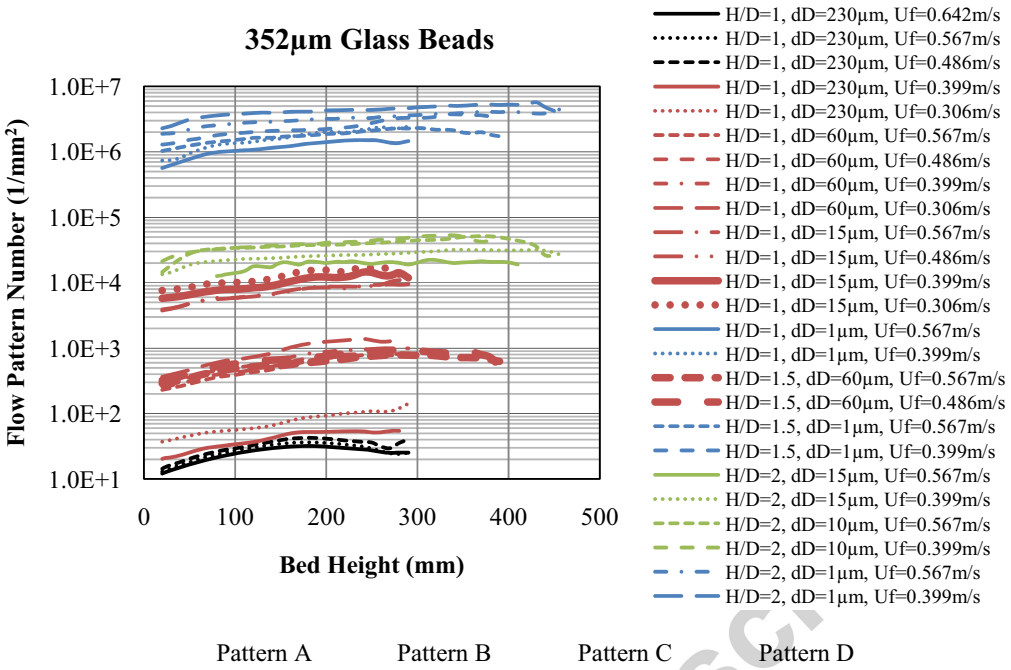

Figure 11. Flow Pattern Parameter vs. bed height for glass beads.

From the FPP expression (Eq. 9), we can identify a flow pattern in the fluidized bed as long as the FPP value is in the range covered by the required pattern. The FPP is equal to bed aspect ratio times the absolute speed of particle, and then divided by the squared pore size of air distributor and excess gas velocity. From equation 9, it can be seen that the pore size of air distributor has a greater effect on FPP. A slight modification of the pore size will significantly change the FPP value, and will alter the flow pattern. When the absolute velocity and other factors are fixed, increase in the excess gas velocity will decrease the FPP value, and an increase of aspect ratio will increase the FPP value.

Figure 12 shows an example for how to identify solid flow pattern based on excess gas velocity ($u-u_{mf}$), the pore size of air distributor and the average kinetic energy per unit mass of particles. In general, the pore size of air distributors has a dominant effect on the FPP. Small change in the pore size will result in a significant change in

FPP, therefore different flow patterns. For example, the FPP is in an order of 10^6 to 10^7 when the pore size is 1μm, and will be reduced to the order of 10^4 to 10^5 when pore size is 10 μm. When the pore size of air distributors is fixed, increasing excess gas velocities ($u-u_{mf}$) will results in a decrease in FPP value, and sometimes a change in solid flow patterns as well.. For example, when the pore size of air distributor is 0.23 mm, the increase in excess gas velocity will change the flow pattern from A to B. However when the pore size of air distributor is 1 μm, the increase in excess gas velocity will slightly decrease the FPP value, but do not change the flow pattern within the experiments conditions presented in this study. Figure 12 also clearly indicate that the solid flow pattern varies with the pore size of air distributor even though the measured particle kinetic energy is the same. Under the same excess gas velocities ($u-u_{mf}$) and the same pore size of the air distributor, higher 'v^2' will results in a slight high FPP value. At the certain average particle kinetic energy (v^2) and a certain pore size of air distributor, low excess gas velocity gives large FPP value. The border lines for flow pattern zone were found from PEPT experiments. There was a blank zone between pattern D zone and pattern C zone. This was due to a big difference between the smallest FPP value of pattern D and the largest FPP value of pattern C. We does not have experimental data to cover this blank zone within the conditions in this study. Overall, the FPP can be potentially developed as a means to identify fluidization behaviour for Geldart B particles within the bubbling regime when the bed aspect ratio is from 1 to 2 units. Further experimental works will be designed to generate a more universal dimensionless FPP number for wide operational conditions and materials, and to remove the particle velocity from FPP number, as well as to find out a more accurate border line between flow pattern C zone and D zone.

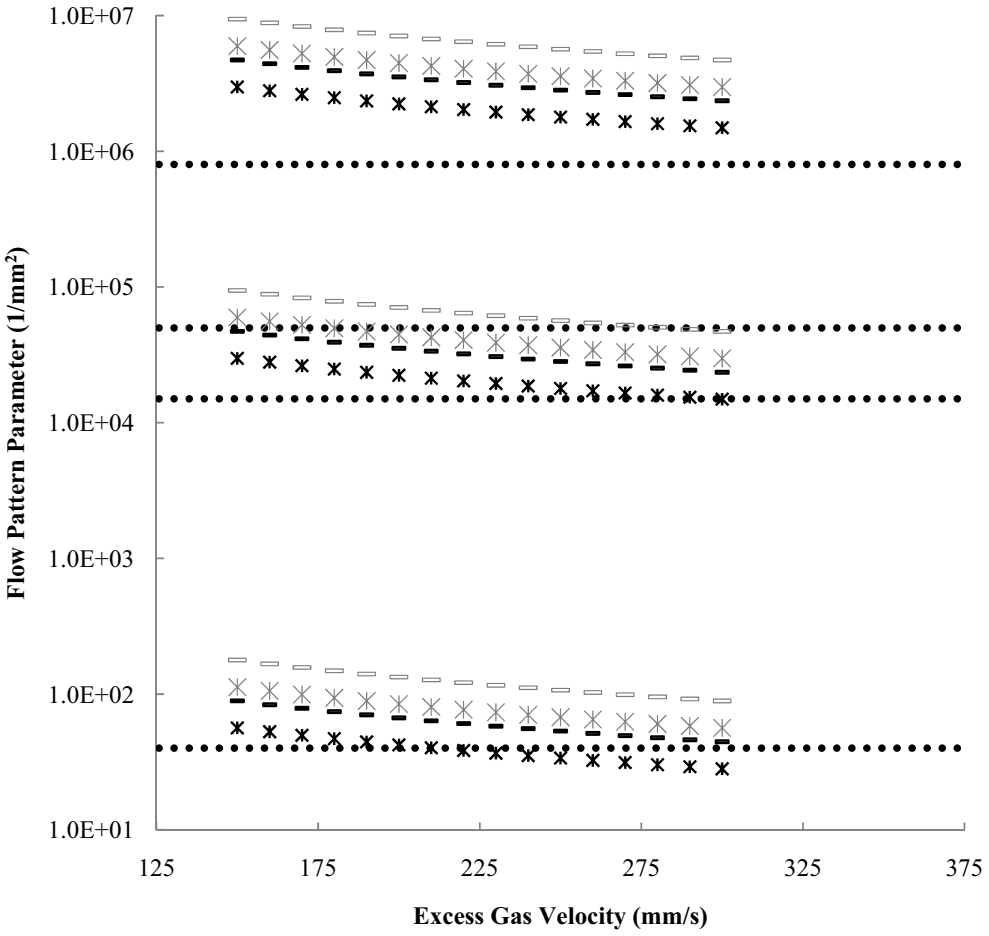

Figure 12. FPP vs. excess gas velocity ($u-u_{mf}$) for a known average kinetic energy of particles, where particle kinetic energy (v^2) for ✱✱✱✱ (H/D=1) and ✳✳✳✳ (H/D=2) are 2.0×10^{-4} $(m/s)^2$, for ▬▬▬▬ (H/D=1) and ▭▭▭▭ (H/D=2) are 5×10^{-4} $(m/s)^2$.

5. Conclusions

Four flow patterns have been found within the bubbling fluidization regime by using the PEPT technique. Pattern A gives poor gas and solid contact and mixing, and should be avoided as possible. Pattern B and pattern C can be considered as acceptable flow structures. While, pattern D can be considered as a desirable flow structure and gives good gas-solid contact and mixing as well as better heat and mass

transfer. Pattern D will benefit the industrial process with high efficiency and product quality.

The flow patterns are a result of a combination of operational conditions, properties of bed materials, and bed designs. A 'Flow Pattern Parameter (FPP)' has been proposed to identify the flow pattern in a bubbling fluidized bed based on PEPT experimental data rather than computational simulation. The FPP combines the effect of particle kinetic energy, minimum fluidization velocity, the superficial gas velocity, the pore size of air distributor, the bed aspect ratio (H/D). The FPP gives a clear classification of different flow patterns. Each flow pattern falls into a specific range of FPP value. Different flow patterns can be identified by the FPP value. It can provide some useful information for the operation control and benefit to academic research and industrial sectors to optimise their productions. However, the FPP presented here is still at its initial stage. Further development is required to generate a more universal dimensionless FPP number for wide operational conditions and materials. The new FPP number will be only a combination of operational conditions, bed design and particle properties.

Acknowledgements

We would like to thank the technical support and advice from Professor David J Parker and Mr Mike D Smith in Birmingham Positron Emission Centre, The of Birmingham, UK.

References

Clift, R., Seville, J.P.K., 1993. Gas cleaning at high temperatures. Blackie Academic & Professional.

Cloete, S., Zaabout, A., Johansen, S.T., Annaland, M.V., Gallucci, F., Amini, S., 2013. The generality of the standard 2D TFM approach in predicting bubbling fluidized bed hydrodynamics. Powder Technology 235, 735-746.

Di Maio, F.P., Di Renzo, A., Vivacqua, V., 2013. Extension and validation of the particle segregation model for bubbling gas-fluidized beds of binary mixtures. Chemical Engineering Science 97, 139-151.

Ding, Y.L., Wang, Z.L., Wen, D.S., Ghadiri, M., Fan, X.F., Parker, D., 2006. Solids behaviour in a dilute gas-solid two-phase mixture flowing through monolith channels. Chemical Engineering Science 61, 1561-1570.

Fan, X., Parker, D.J., Smith, M.D., 2006a. Enhancing F-18 uptake in a single particle for positron emission particle tracking through modification of solid surface chemistry. Nuclear Instruments & Methods in Physics Research Section a-Accelerators Spectrometers Detectors and Associated Equipment 558, 542-546.

Fan, X., Parker, D.J., Smith, M.D., 2006b. Labelling a single particle for positron emission particle tracking using direct activation and ion-exchange techniques. Nuclear Instruments & Methods in Physics Research Section a-Accelerators Spectrometers Detectors and Associated Equipment 562, 345-350.

Fan, X., Parker, D.J., Yang, Z., Seville, J.K.P., Fan, X., Parker, D.J., Yang, Z., Seville, J.K.P., 2006c. A Simple and Selective Method for Separation of Trace 61Cu from Nickel Solutions. Nuclear Medicine and Biology 33, 939-944.

Fan, X.F., Parker, D.J., Yang, Z.F., Seville, J.P.K., Baeyens, J., 2008a. The effect of bed materials on the solid/bubble motion in a fluidised bed. Chemical Engineering Science 63, 943-950.

Fan, X.F., Yang, Z.F., Parker, D.J., 2011. Impact of solid sizes on flow structure and particle motions in bubbling fluidization. Powder Technology 206, 132-138.

Fan, X.F., Yang, Z.F., Parker, D.J., Armstrong, B., 2008b. Prediction of bubble behaviour in fluidised beds based on solid motion and flow structure. Chemical Engineering Journal 140, 358-369.

Fotovat, F., Chaouki, J., Bergthorson, J., 2013. The effect of biomass particles on the gas distribution and dilute phase characteristics of sand–biomass mixtures fluidized in the bubbling regime. Chemical Engineering Science 102, 129-138.

Gómez-Barea, A., Leckner, B., 2010. Modeling of biomass gasification in fluidized bed. Progress in Energy and Combustion Science 36, 444-509.

Garcia-Gutierrez, L.M., Soria-Verdugo, A., Garcia-Hernando, N., Ruiz-Rivas, U., 2013. Simulation of object motion in a bubbling fluidized bed using a Monte Carlo method. Chemical Engineering Science 96, 26-32.

He, Y.R., Lu, H.L., Sun, Q.Q., Yang, L.D., Zhao, Y.H., Gidaspow, D., Bouillard, J., 2004. Hydrodynamics of gas-solid flow around immersed tubes in bubbling fluidized beds. Powder Technology 145, 88-105.

Herzog, N., Schreiber, M., Egbers, C., Krautz, H.J., 2012. A comparative study of different CFD-codes for numerical simulation of gas-solid fluidized bed hydrodynamics. Computers & Chemical Engineering 39, 41-46.

Ku, X.K., Li, T., Lovas, T., 2013. Influence of drag force correlations on periodic fluidization behavior in Eulerian-Lagrangian simulation of a bubbling fluidized bed. Chemical Engineering Science 95, 94-106.

Kunii, D., Levenspiel, O., 1991. Fluidization engineering, 2nd ed. Butterworth-Heinemann, Boston.

Laverman, J.A., Fan, X., Ingram, A., Annaland, M.V., Parker, D.J., Seville, J.P.K., Kuipers, J.A.M., 2012. Experimental study on the influence of bed material on the scaling of solids circulation patterns in 3D bubbling gas-solid fluidized beds of glass and polyethylene using positron emission particle tracking. Powder Technology 224, 297-305.

Mychkovsky, A.G., Ceccio, S.L., 2012. LDV measurements and analysis of gas and particulate phase velocity profiles in a vertical jet plume in a 2D bubbling fluidized bed Part III: The effect of fluidization. Powder Technology 220, 37-46.

Olsson, J., Pallares, D., Johnsson, F., 2012. Lateral fuel dispersion in a large-scale bubbling fluidized bed. Chemical Engineering Science 74, 148-159.

Parker, D.J., Allen, D.A., Benton, D.M., Fowles, P., McNeil, P.A., Tan, M., Beynon, T.D., 1997. Developments in particle tracking using the Birmingham Positron Camera. Nuclear Instruments & Methods in Physics Research Section a-Accelerators Spectrometers Detectors and Associated Equipment 392, 421-426.

Parker, D.J., Broadbent, C.J., Fowles, P., Hawkesworth, M.R., Mcneil, P., 1993. Positron Emission Particle Tracking - a Technique for Studying Flow within Engineering Equipment. Nuclear Instruments & Methods in Physics Research Section a-Accelerators Spectrometers Detectors and Associated Equipment 326, 592-607.

Saayman, J., Nicol, W., Van Ommen, J.R., Mudde, R.F., 2013. Fast X-ray tomography for the quantification of the bubbling-, turbulent- and fast fluidization-flow regimes and void structures. Chemical Engineering Journal 234, 437-447.

Salman, A.D., Hounslow, M.J., 2007. Fluidized bed applications - Preface. Chemical Engineering Science 62, 1-1.

Sedighikamal, H., Zarghami, R., 2013. Dynamic characteristics of bubbling fluidization through recurrence rate analysis of pressure fluctuations. Particuology 11, 282-287.

Shi, Z.S., Wang, W., Li, J.H., 2011. A bubble-based EMMS model for gas-solid bubbling fluidization. Chemical Engineering Science 66, 5541-5555.

Shibata, K., Shimizu, M., Inaba, S.-i., Takahashi, R., Yagi, J.-i., 1991. Pressure Loss and Hold-up Powders for Gas-Powder Two Phase Flow in Packed Beds. ISIJ International 31, 434-439.

Smolders, K., Baeyens, J., 2001. Gas fluidized beds operating at high velocities: a critical review of occurring regimes. Powder Technology 119, 269-291.

Soria-Verdugo, A., Garcia-Gutierrez, L.M., Sanchez-Delgado, S., Ruiz-Rivas, U., 2011. Circulation of an object immersed in a bubbling fluidized bed. Chemical Engineering Science 66, 78-87.

Vakhshouri, K., Grace, J.R., 2010. Effects of the plenum chamber volume and distributor geometry on fluidized bed hydrodynamics. Particuology 8, 2-12.

Wang, J.W., van der Hoef, M.A., Kuipers, J.A.M., 2011. The role of scale resolution versus inter-particle cohesive forces in two-fluid modeling of bubbling fluidization of Geldart A particles. Chemical Engineering Science 66, 4229-4240.

Wang, Y., Zou, Z., Li, H., Zhu, Q., 2013. A new drag model for TFM simulation of gas–solid bubbling fluidized beds with Geldart-B particles. Particuology.

Wardag, A.N.K., Larachi, F., 2012. Bed expansion and disengagement in corrugated-wall bubbling fluidized beds. Chemical Engineering Science 81, 273-284.

Weber, J.M., Mei, J.S., 2013. Bubbling fluidized bed characterization using Electrical Capacitance Volume Tomography (ECVT). Powder Technology 242, 40-50.

Xiong, Q.G., Deng, L.J., Wang, W., Ge, W., 2011. SPH method for two-fluid modeling of particle-fluid fluidization. Chemical Engineering Science 66, 1859-1865.

Yang, Z., Fan, X., Fryer, P.J., Parker, D.J., Bakalis, S., 2007a. Improved multiple-particle tracking for studying flows in multiphase systems. Aiche Journal 53, 1941-1951.

Yang, Z., Fryer, P.J., Bakalis, S., Fan, X., Parker, D.J., Seville, J.P.K., 2007b. An improved algorithm for tracking multiple, freely moving particles in a Positron Emission Particle Tracking system. Nuclear Instruments & Methods in Physics Research Section a-Accelerators Spectrometers Detectors and Associated Equipment 577, 585-594.

Highlights

- ✧ Experiments conducted in a 3D gas/solid fluidized bed via the PEPT technique.
- ✧ Four flow structures within the bubbling regime.
- ✧ Flow Pattern Parameter has been developed.
- ✧ Flow Pattern Parameter can control and predict the fluidization performance.

Graphical Abstract (for review)

Predict and control solid flow patterns using Flow Pattern Parameter

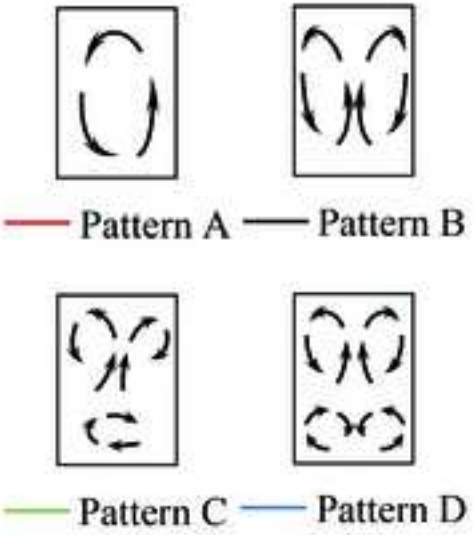

$$FPP = \frac{|v| \times H_B}{D_B \times {d_D}^2 \times (u_f - u_{mf})}$$

v-particle speed (mm/s), uf-superficial gas velocity (mm/s), HB-bed height (mm), umf-minimum fluidization velocity (mm/s), DB-bed diameter (mm), dD-pore size of air distributor (mm)

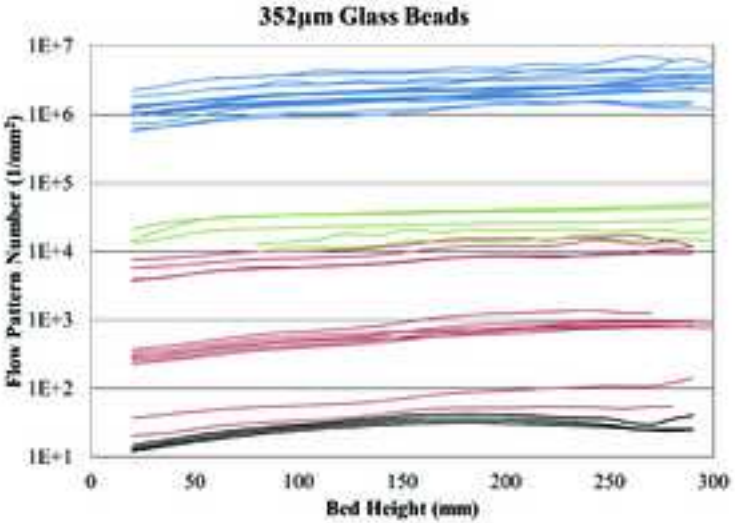

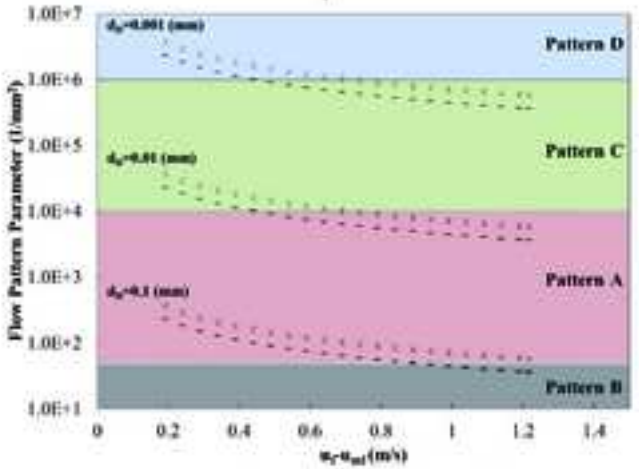

----- : $v^2 = 2.0\times10^{-4}$ (m/s)^2

xxxx : $v^2 = 5.0\times10^{-4}$ (m/s)^2